BIOCHEMISTRY
including biophysical chemistry & molecular biology

Article

pubs.acs.org/biochemistry

Allosteric Inhibition of Human Ribonucleotide Reductase by dATP Entails the Stabilization of a Hexamer

Nozomi Ando,[*,†,‡,#,⊥] Haoran Li,[‡,#] Edward J. Brignole,[†,‡] Samuel Thompson,[‡] Martin I. McLaughlin,[‡] Julia E. Page,[‡] Francisco J. Asturias,[∥] JoAnne Stubbe,[‡,§] and Catherine L. Drennan[*,†,‡,§]

[†]Howard Hughes Medical Institute, [‡]Department of Chemistry, and [§]Department of Biology, Massachusetts Institute of Technology, Cambridge, Massachusetts 02139, United States

[∥]Department of Integrative Structural and Computational Biology, The Scripps Research Institute, La Jolla, California 92037, United States

Supporting Information

ABSTRACT: Ribonucleotide reductases (RNRs) are responsible for all de novo biosynthesis of DNA precursors in nature by catalyzing the conversion of ribonucleotides to deoxyribonucleotides. Because of its essential role in cell division, human RNR is a target for a number of anticancer drugs in clinical use. Like other class Ia RNRs, human RNR requires both a radical-generation subunit (β) and nucleotide-binding subunit (α) for activity. Because of their complex dependence on allosteric effectors, however, the active and inactive quaternary forms of many class Ia RNRs have remained in question. Here, we present an X-ray crystal structure of the human α subunit in the presence of inhibiting levels of dATP, depicting a ring-shaped hexamer (α_6) where the active sites line the inner hole. Surprisingly, our small-angle X-ray scattering (SAXS) results indicate that human α forms a similar hexamer in the presence of ATP, an activating effector. In both cases, α_6 is assembled from dimers (α_2) without a previously proposed tetramer intermediate (α_4). However, we show with SAXS and electron microscopy that at millimolar ATP, the ATP-induced α_6 can further interconvert with higher-order filaments. Differences in the dATP- and ATP-induced α_6 were further examined by SAXS in the presence of the β subunit and by activity assays as a function of ATP or dATP. Together, these results suggest that dATP-induced α_6 is more stable than the ATP-induced α_6 and that stabilization of this ring-shaped configuration provides a mechanism to prevent access of the β subunit to the active site of α.

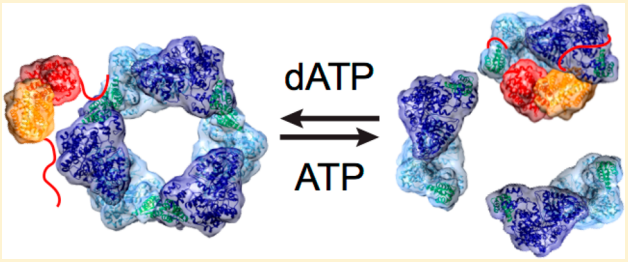

Found in all organisms, RNRs are complex allosteric enzymes that supply precursors for DNA replication and repair at controlled levels needed for maintaining the fidelity of these processes.[1−3] Because of their essential role in DNA biosynthesis, RNRs are excellent targets for anticancer, antiviral, and antiparasitic drugs. In particular, human RNR is the target for a number of inhibitors that are currently in clinical use for chemotherapy.[4,5] However, despite their medical importance, the lack of structural information on the active and inactive forms of many of these enzymes presents a major challenge in the design of new therapeutics.

RNRs are classified by the metallocofactor essential for initiating the intricate, radical-mediated mechanism of nucleotide reduction.[6,7] Eukaryotes and many aerobic bacteria utilize class Ia RNRs, which require two subunits, α and β, for activity (Figure 1A). α contains three nucleotide-binding sites, while β harbors a diferric-tyrosyl radical cofactor (Y176• in human RNR). For each turnover, the two subunits associate and engage in a long-range radical transfer process over 35 Å, involving multiple proton-coupled electron transfer (PCET) steps and redox active amino acids. In this process, the Y• cofactor in β oxidizes a conserved cysteine in the active site of α to generate a thiyl radical that initiates nucleotide reduction via a conserved mechanism.[8] Class Ia RNRs can reduce any of the four ribonucleoside 5′-diphosphates (ADP, CDP, UDP, GDP) that bind to the active site of α, whereas substrate specificity is controlled by the binding of deoxyribonucleoside 5′-triphosphates (dATP, TTP, dGTP) and adenosine triphosphate (ATP) to an allosteric site in α known as the specificity site (Figure 1A). Both ATP and dATP can promote CDP reduction when bound to the specificity site. However, their binding at a second allosteric site in the so-called N-terminal cone domain of α modulates the overall rate of reduction (Figure 1A, green domains). Binding of ATP at this activity site stimulates nucleotide reduction, whereas dATP inactivates the enzyme. Together, these allosteric sites act to maintain the proper balance of intracellular deoxyribonucleotide pools.

In recent years, the role of the oligomerization state in the allosteric regulation of class Ia RNRs has been a central question.[9−17] In all class Ia RNRs examined to date, β is a stable dimer (β_2). In the case of the most studied class Ia RNR from *Escherichia coli*, α is also a dimer (α_2) when effectors are bound

Received: November 7, 2015
Revised: December 11, 2015
Published: December 21, 2015

DOI: 10.1021/acs.biochem.5b01207
Biochemistry 2016, 55, 373−381

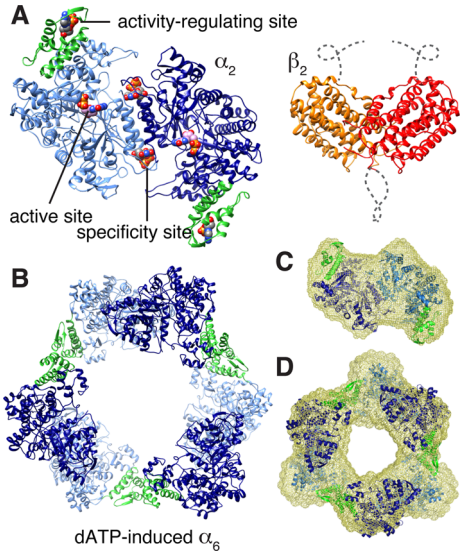

Figure 1. Structures of human RNR. (A) Each monomer of human α_2 contains three nucleotide-binding sites (PDB: 3HNC, 3HND, 3HNE). The activity-regulating site is housed in the N-terminal cone domain (colored in green). Both the C-terminus and N-terminus are disordered in structures of β_2 (dotted lines, PDB: 2UW2). (B) Crystal structure of human dATP-induced α_6 determined in this study. (C) Scattering from 4 μM α in the presence of 1 mM CDP yields an ab initio shape reconstruction (yellow) that is consistent with the crystal structure of human α_2. (D) Scattering from 4 μM α in the presence of 50 μM dATP and 1 mM CDP yields a shape reconstruction (yellow) that is consistent with the crystal structure of human α_6.

to the specificity site. Recent studies on *E. coli* RNR have demonstrated that, as originally proposed,[18] α_2 and β_2 assemble into a compact but transient $\alpha_2\beta_2$ complex, which is active for turnover.[9,14] In contrast, the binding of dATP at inhibitory concentrations to the N-terminal cone domains leads to the formation of an unusual ring-shaped $\alpha_4\beta_4$ complex in *E. coli* RNR,[9,19] in which each β_2 is held at "arm's length" from the active sites of α_2, preventing radical transfer and hence inhibiting the enzyme. However, despite structural homology across all class Ia RNRs, eukaryotic RNRs do not form the same quaternary structures as the *E. coli* enzyme. Early analytical ultracentrifugation (AUC) studies showed that both ATP and dATP induce higher order oligomers of mammalian RNRs containing only the α subunit,[20,21] in contrast to *E. coli* RNR, which require both subunits to form oligomers.[22,23] The role of oligomerization in mammalian α was later revisited by Cooperman and co-workers with dynamic light scattering (DLS) and AUC. In these studies, they observed large oligomers, which they attributed to α_4 formation in the presence of dATP and α_6 in the presence of high ATP (10 mM).[11,13] Although α tetramerization in eukaryotic RNRs has not been reported since, α hexamerization has been reported in the presence of both activating and inactivating effectors by multiple mass-estimation techniques, including size-exclusion chromatography (SEC),[10,12,15] gas-phase electrophoretic mobility analysis (GEMMA),[16] and multiangle light scattering (MALS).[12] These observations have led to the proposal that α_6 can be active or inactive, depending on the effectors that are bound.[12]

Structural studies targeted at elucidating the quaternary structure of eukaryotic RNRs have been challenging and thus far limited to inhibitory conditions. Notably, in a recent study by Fairman et al., cocrystallization of *Saccharomyces cerevisiae* α with dATP led to a crystal lattice that could be formed by two different hexameric arrangements of α (Protein Data Bank or PDB entry 3PAW), one in which three copies of α_2 form a ring with the active sites facing inward (Figure S1A) and another in which three copies of α_2 form an inverted structure with the active sites facing outward (Figure S1B).[12] In the same study, mutagenesis on human α and electron microscopy (EM) data on *Saccharomyces cerevisiae* α supported the ring-shaped structure with the inward-facing active sites (Figure S1A) as the dATP-inhibited form of α_6. On the basis of mutagenesis and tryptophan fluorescence quenching data, it was further proposed that the ATP-induced α_6 configuration would have a different packing arrangement than that formed with dATP. However, no structural characterizations in the presence of ATP were reported. Also, this study relied on the *S. cerevisiae* enzyme for their structural studies of the α_6 state.

In this present study, we investigate the quaternary structure of human RNR using three complementary structural techniques. We present the first X-ray crystal structure of a dATP-induced α_6 from human RNR. The crystal lattice giving rise to this structure supports only one hexameric arrangement, in which the active sites face inward. By measuring small-angle X-ray scattering (SAXS) at increasing concentrations of dATP and ATP, we further provide evidence that this hexameric arrangement forms in solution from the dimeric state in the case of both effectors. At high ATP concentrations (>1 mM), however, the ATP-induced α_6 readily interconverts with a newly identified filament state, which we describe by both SAXS and electron microscopy. Addition of β_2 also promotes large-scale structural changes to α_6 in the presence of ATP, but not dATP. Although the physiological relevance of the filament state is not known, our results show that the human α subunit can readily accommodate multiple structural states in the presence of ATP and β_2. These results support a unified mechanism of allosteric inhibition for the class Ia RNRs, in which dATP is the only effector that favors stabilization of a single conformation, one in which β_2 likely has limited access to the active sites of α_6.

EXPERIMENTAL PROCEDURES

Protein Expression and Purification. His_6-tagged human α and β were isolated using a modified procedure from previous studies,[10,15] while β was reconstituted following published protocols with minor modifications.[15] To remove the N-terminal His_6-tag from as-purified α, 2 U thrombin (Novagen) was mixed with 1 mg α, followed by incubation at 4 °C for 6−8 h. Removal of the His_6 tag was previously shown to have a negligible effect on the specific activity of α,[10] and hence, the tagged and untagged α constructs are interchangeable with the one exception being the fraction of filaments at high ATP concentration (as discussed in the Results). In the case of human β, which is prone to proteolysis, the His_6 tag was kept intact to aid in the purification of full-length β from fragments. For additional details, see Supporting Information.

RNR Activity Assay. The activity of His_6-tagged α or β was determined by measuring the reduction of [5-^{3}H] CDP in the presence of 5-fold excess of the other subunit. To correlate activity with the SAXS studies, 4 μM α (or β) was added to an assay mixture containing 20 μM β (or α), 2 mM [5-^{3}H] CDP, 3 mM ATP, 25 μM human thioredoxin 1 (hTrx1), 0.2 μM human thioredoxin reductase 1 (hTrxR1), 2 mM NADPH in a

DOI: 10.1021/acs.biochem.5b01207
Biochemistry 2016, 55, 373−381

modified assay buffer (50 mM HEPES, 5% glycerol, 15 mM $MgCl_2$, 150 mM KCl, pH 7.6). Before mixing, all the components were preincubated at 37 °C for 1 min. After initiation by [5-^{3}H] CDP addition, the 180-μL reaction mixture was incubated at 37 °C for 2 min, and a 40-μL aliquot was quenched by boiling for 2 min. Four aliquots were taken at 0.5, 1.0, 1.5, and 2.0 min, respectively. After centrifugation, the supernatant (36 μL) was transferred to a new tube, and the dephosphorylation reaction was performed by incubation at 37 °C for 2 h with 14 U calf alkaline phosphatase (Roche) and 400 nmol of carrier deoxycytidine (dC) in dephosphorylation buffer (75 mM Tris-HCl, 0.15 mM EDTA, pH 8.5). The amount of dC was quantified as described previously.[24] In addition, for assaying α at other concentrations (0.5, 1, 10 μM), the [α]:[β] ratio was kept at 1:5 for all experiments to facilitate comparison of α activities, while [CDP] was varied in order to ensure substrate saturation (Table S1).

Crystallography. Protein solutions containing 12 mg/mL His_6-tagged α in 50 mM HEPES pH 7.6, 15 mM $MgCl_2$, 100 mM KCl, 10 mM DTT, 5% v/v glycerol, 500 μM dATP, and 3 mM CDP were prepared on ice and incubated at 37 °C for 2 min. Crystallization experiments were then performed by hanging drop vapor diffusion at 18 °C. Protein solution (1 μL) was mixed with precipitant solution (1 μL) containing 100 mM HEPES pH 7.0, 32% v/v Jeffamine M600, and 10 mM DTT and suspended over a 400 μL reservoir of precipitant solution. Crystals appeared within a week and were flash cooled in liquid N_2 without additional cryoprotection. Diffraction images were collected at the Cornell High Energy Synchrotron Source (CHESS) F1 Station on an ADSC Quantum 270 CCD detector, indexed and integrated with XDS, and scaled with XSCALE (Table S2).[25] The structure was solved to 9 Å resolution by molecular replacement in Phaser[26] using a previously solved structure of α_2 (3HNC chains A and B) with all waters and ligands removed as the search model. A solution with one α_2 in the asymmetric unit was found. Refinement at 9 Å resolution was performed in PHENIX[27] using four atom groups for both rigid body and group B-factor refinement: for each α chain, the N-terminal domain (residues 1−90) and the rest of the polypeptide (residues 91−742) (Table S2). Refinement beyond rigid body was not carried out due to the low resolution. Coordinates and structure factors have been deposited in the PDB as entry 5D1Y.

Small-Angle X-ray Scattering. SAXS was performed at the CHESS G1 station using a 10.5 keV 250 μm × 250 μm X-ray beam. Data were collected on a Pilatus 100 K detector with a sample-to-detector distance of 1.5 m. The transmitted intensity was measured on a PIN diode beamstop, as previously described.[25] SAXS measurements on His_6-tagged α were performed in the standard in vitro assay buffer (50 mM HEPES, pH 7.6, 15 mM $MgCl_2$, 5% glycerol). All other SAXS measurements were performed with untagged α or His_6-tagged β in a modified assay buffer (50 mM HEPES, pH 7.6, 15 mM $MgCl_2$, 5% glycerol, 13 mM KCl). Each α sample was prepared by first incubating solutions of α, CDP, and ATP (or dATP) separately at 37 °C for 1 min, then adding CDP and ATP (or dATP), in that order, to the α solution. The mixed solution was then equilibrated by incubating at 37 °C for 1 min, followed immediately by data collection. Samples containing both subunits were prepared in a similar way, except that DTT was added to the α stock solution to bring the final DTT concentration in the reaction mixture to 5 mM. CDP and ATP (or dATP) were added to the α stock solution in the same manner as described above. β (preincubated for 30 s at 37 °C) was then added, and data collection was initiated within 30 s of mixing. For every sample, a carefully matched background solution was prepared containing all ingredients in the protein buffer. Samples were loaded into an *in vacuo* oscillating flow cell,[26] and multiple 1 and 5 s exposures were taken per sample as previously described.[27] Data collection was completed within 4 min of loading each sample. The scattering images were integrated about the beam center and normalized by the transmitted intensities following previously described image correction procedures.[27] Superimposable exposures that did not display apparent radiation-induced changes were averaged. Background scattering collected on matched buffer was subtracted from the protein solution scattering to produce the one-dimensional protein scattering profile, $I(q)$, as a function of q, where $q = 4\pi/\lambda \sin \theta$; 2θ is the scattering angle, and λ is the X-ray wavelength. The quality of the background subtraction was evaluated as described previously.[27]

Analysis of structural parameters, singular value decomposition analysis, and multistate fitting of experimental scattering curves were performed using custom code written in MATLAB, as described previously.[9,28] The zero-angle scattering intensity $I(0)$ and overall radius of gyration R_g were obtained from a Guinier approximation (eq 1)[29] to the low q region of the scattering profiles. R_g and $I(0)$ are determined from linear fits to Guinier plots, $\ln(I(q))$ versus q^2, in the region $q_{max}*R_g < 1.3$.

$$I(q) \approx I(0) \exp(-R_g^2 q^2/3) \quad (1)$$

In the case of elongated proteins (e.g., filaments), a similar approximation can be made to $I(q)*q$ (eq 2).[29] Here, a cross-sectional radius of gyration, R_c, can be determined from a linear fit to the cross-sectional Guinier plot, $\ln(I(q)*q)$ versus q^2.

$$I(q)*q \approx I(0) \exp(-R_c^2 q^2/2) \quad (2)$$

For conformationally homogeneous samples, the pair distance distribution function, $P(r)$, was calculated from the experimental $I(q)$ with the indirect Fourier transform method[29] implemented in the program GNOM.[30] Low-resolution models of protein structures were generated from the GNOM outputs (with a high-resolution limit of $qR_g \approx 8$) using the *ab initio* reconstruction programs DAMMIF[31] and DAMMIN.[32] DAMAVER[33] was used to align *ab initio* models, reject outliers, and average the remaining models to produce the most probable model. Structural parameters and shape reconstruction statistics are summarized in Table S3. Theoretical scattering curves were calculated from atomic coordinates using FoXS.[34] The disordered C-terminus of α (residues 743−792) and several other missing residues (292−293) were modeled into the structure of the dATP-induced α_6 with Modeller,[35] and conformational sampling was performed with constant-temperature molecular dynamics (300 K) in AllosMod-FoXS.[36] In the model that best fit the SAXS data, the C-terminal tails were allowed to relax and take up space within the α_6 ring.

Electron Microscopy. Specimens for electron microscopy were prepared by incubating 6 μM α with 1, 3, or 10 mM ATP in assay buffer at 37 °C for 2 min followed by 20-fold dilution in assay buffer containing a matched concentration of ATP. The diluted mixture (5 μL) were applied to a thin carbon film supported by a 300 mesh Cu/Rh grid (Ted Pella) that had been glow discharged immediately before use.[37] The grid was

DOI: 10.1021/acs.biochem.5b01207
Biochemistry 2016, 55, 373−381

washed three times with a stain solution containing 2% uranyl acetate (Ted Pella) and 0.2% trehalose. A second carbon layer was applied, excess stain blotted with filter paper, and the specimen air-dried following standard protocols.[38] Images were acquired at 50000× magnification on a Tecnai F20 microscope (FEI) operated at 120 kV equipped with a 4096 × 4096 pixel CCD camera (Gatan).

RESULTS

Crystal Structure of the dATP-Induced Hexamer. The subunit arrangement of the dATP-induced α_6 was determined by X-ray crystallography. Although crystallization of human α in the presence of dATP has been documented, the structure could not be solved due to poor diffraction.[12] We find that in agreement with previous observations,[12] cocrystallization of human α with 500 μM dATP yields crystals that diffract to very low resolution (~8 Å), much of which is masked by the beamstop in a typical macromolecular crystallography beamline. However, by utilizing a small beamstop to collect diffraction data at low resolution, a 9-Å structure could be solved by molecular replacement using a previously reported human α_2 structure as the search model (PDB: 3HNC)[12] (Table S2). At this low resolution, structural details such as side chain and ligand positions cannot be inferred. However, the subunit arrangement can be determined unambiguously (Figure S2). The final structure reveals a ring-shaped α_6 (Figure 1B) formed by three α_2 subunits making contacts at the N-terminal cone domains containing the activity-regulating site that binds dATP (Figure 1B, green). Importantly, the crystal lattice giving rise to this new structure supports only one hexameric arrangement, one that is similar to the inward-pointing architecture in the 6.6-Å resolution structure of the dATP-induced α_6 from *S. cerevisiae* RNR[12] (Figure S1A). The human dATP-induced α_6 structure also shares features with the dATP-inhibited $\alpha_4\beta_4$ complex from *E. coli*,[9,19] which is a ring of a similar size with the active sites facing inward. As in the human α_6, the N-terminal cone domains are also involved in making the subunit contacts in this *E. coli* structure.

dATP and ATP Produce Similar Hexamers. With the structure of the dATP-induced human α_6 determined, SAXS was employed to compare the structural effects of ATP and dATP on human α in solution. SAXS is a solution-based structural technique that is uniquely suited for investigating quaternary structure under varying solution conditions, particularly when mixtures of species may be present.[9] Using an in-vacuum oscillating flow cell, scattering was measured from α at very dilute concentrations close to the physiological range (0.5−1 μM monomer).[39] All samples contained 1 mM CDP, the natural substrate for both ATP and dATP when bound to the specificity site.

Titration of dATP into 4 μM α in the presence of 1 mM CDP leads to a dramatic change in the shape of the scattering curves and a concomitant increase in the zero-angle scattering intensity (Figure 2A, blue to red), indicative of a large structural change involving an increase in mass. Over the course of the dATP titration, much of the structural change occurs at low μM dATP. Above 8 μM dATP, the scattering curves are nearly superimposable. The large set of scattering curves allows for the determination of the number of interconverting species in a model-independent manner via singular value decomposition (SVD). Consistent with the presence of iso-scattering points (Figure 2A), SVD produces two significant singular vectors (Figure S3, magenta), suggesting that the structural change

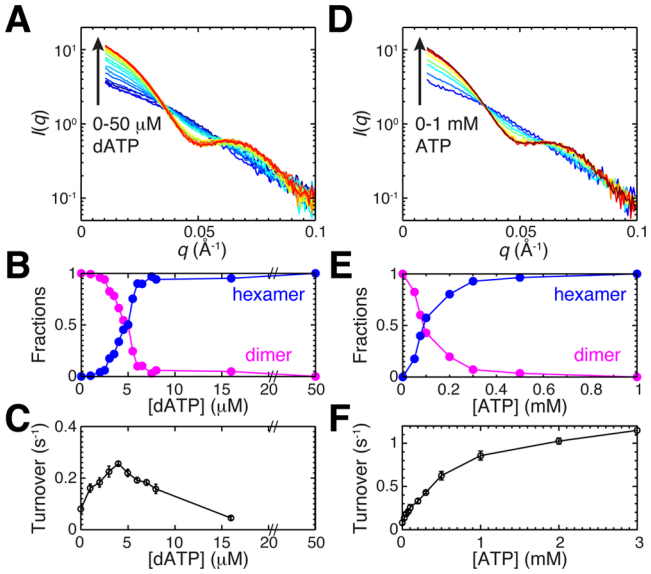

Figure 2. Both dATP and low ATP induce hexamerization of human α. (A) SAXS profiles measured as 0−50 μM dATP is titrated into 4 μM α in the presence of 1 mM CDP (blue to red curves) display isointensity points, suggesting a two-state transition. (B) Fitting linear combinations of α_2 and α_6 scattering to the titration data provides relative fractions of the two species and shows a midpoint near equimolar [dATP]:[α]. (C) Activity in the presence of dATP is biphasic with a loss in activity beyond equimolar [dATP]:[α]. (D) SAXS profiles measured as 0−1 mM ATP is titrated into 4 μM α in the presence of 1 mM CDP (blue to red curves) are consistent with a two-state dimer−hexamer transition. (E) Fitting linear combinations of α_2 and α_6 scattering to the titration data provides relative fractions of the two species as a function of ATP. (F) A steady increase in activity is observed up to 1 mM ATP and continues to slowly increase at higher ATP.

caused by dATP is an interconversion of two oligomerization states. The initial state (at 0 μM dATP) agrees well with known crystal structures of the dimer (Figures 1C and S5A), whereas the final state (above 8 μM dATP) agrees well with the crystal structure of the human hexamer (Figures 1D and 5B). Interestingly, although mammalian α has been reported to dissociate in the absence of effectors,[13,15,16] we find that substrate binding is sufficient to induce dimerization, possibly due to reduced conformational disorder. Linear combinations of the scattering at 0 μM dATP and at 50 μM dATP fit well to the set of curves shown in Figure S6A, thus indicating that the structural change caused by dATP can be described as a dimer−hexamer transition with a midpoint near the equimolar point (1 dATP per α) (Figure 2B). Only hexamers are observed above 8 μM, which corresponds to the full occupancy point (2 dATP's per α). Importantly, intermediates, including α tetramers, are not observed in these data.

Under identical solution conditions, ATP was titrated into 4 μM α in the presence of 1 mM CDP. Addition of ATP up to 1 mM leads to scattering curves (Figure 2D, blue to red) that are highly similar to the set obtained from the dATP titration experiment (Figure 2A). SVD of these ATP titration data also yields two significant singular vectors, indicative of a two-state transition that is largely complete at 1 mM ATP (Figure S4, magenta). Notably, the calculated scattering of an inverted hexamer model in which the active sites point outward (Figure S1B) yields a poor fit to the scattering data at 1 mM ATP (Figure S5B). In contrast, the scattering at 1 mM ATP is nearly

DOI: 10.1021/acs.biochem.5b01207
Biochemistry 2016, 55, 373−381

superimposable (up to a q value of 0.15 Å^{-1}) with that measured in the presence of 50 μM dATP (Figure S5B), suggesting that ATP forms a hexamer that is indistinguishable from the dATP-induced α_6 at low resolution. Furthermore, linear combinations of the same two scattering curves used to fit the dATP titration data also fit well to the ATP titration data (Figure S6B), indicating that sub-millimolar concentrations of ATP cause a dimer−hexamer transition similar to that observed with micromolar concentrations of dATP.

Instability of the ATP-Induced hexamer. Although α hexamerization is favored up to 1 mM ATP (Figure 2D,E), additional conformational changes are observed at higher ATP concentrations. Increasing the ATP concentration to 10 mM in the presence of 4 μM α and 1 mM CDP leads to an upturn in the scattering at low q and a loss of features representing the hexamer, such as the peak at q = 0.07 Å^{-1} arising from cross-ring interference (Figure 3A). These changes are consistent

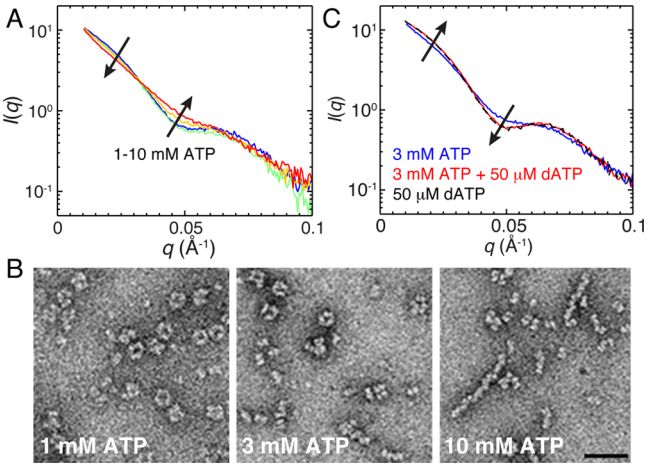

Figure 3. High ATP induces a third α oligomerization state. (A) SAXS profiles measured from 4 μM α in the presence of 1 mM CDP and high ATP (1−10 mM) display changes in scattering (blue to red curves) that can be attributed to the conversion of hexamers into a highly elongated species. (B) Electron micrographs of 0.3 μM His$_6$-tagged α in 1, 3, and 10 mM ATP show the conversion from primarily hexamers to filaments. The scale bar corresponds to 50 nm. (C) The SAXS profile measured from 4 μM α in 3 mM ATP, 1 mM CDP (blue) becomes more defined when 50 μM dATP is added to the mix (red) and becomes superimposable with that of 4 μM α in 50 μM dATP, 1 mM CDP (black dotted). Although subtle, the change in scattering is consistent with the reversal of filaments into hexamers.

with the growth of aggregates that are highly anisotropic in shape. Interestingly, this effect is more pronounced for α constructs with an N-terminal hexahistidine (His$_6$) tag. Although the tag has negligible effects on the dimer−hexamer transitions in the presence of dATP or submillimolar ATP (Figures S3, S4), the presence of the tag leads to a greater fraction of anisotropic aggregates at >1 mM ATP. In fact, the scattering from 4 μM His$_6$-tagged α displays a total loss of features at 10 mM ATP and can be approximated as a highly elongated species with a cross-sectional radius of gyration (R_c) of 28.1 Å (Figure S5C). In agreement with the SAXS data, electron micrographs of 0.3 μM His$_6$-tagged α incubated with 1, 3, and 10 mM ATP illustrate the progressive conversion of hexamers to prominent filaments (Figure 3B). The formation of filaments would explain previous observations of aggregation-like behavior in eukaryotic α occurring in the presence of ATP.[16] Whereas a loss of scattering features is observed at millimolar concentrations of ATP (Figure 3A), these features become more defined when dATP is added to 4 μM α in the presence of 3 mM ATP (Figure 3C), suggesting that the filament formation is reversible. Together, these results demonstrate that the ATP-induced α_6 can readily interconvert with other conformational states, whereas dATP favors the hexameric form.

Activity in the Presence of dATP and ATP. In an effort to correlate oligomerization with the specific activity of α, dCDP formation was measured as a function of dATP and ATP in the presence of 4 μM α, a 5-fold excess of β, 0.5 mM [5-^{3}H]-CDP, human thioredoxin, and human thioredoxin reductase. To prevent precipitation of the subunits at these high concentrations, the assay buffer was modified with the addition of 150 mM KCl. In the absence of dATP or ATP, we find that turnover occurs at a very low rate of 0.080 ± 0.014 s^{-1} (initial points in Figure 2C,F). Titration of dATP leads to a 3.2-fold increase up to 4 μM dATP (equimolar with α), followed by a steady decrease to 0.045 ± 0.007 s^{-1} at 16 μM dATP (Figure 2C). On the basis of previously reported dissociation constants of 0.07 and 1.5 μM for dATP binding to the specificity and activity sites, respectively, in murine RNR,[40] our observation of biphasic behavior in activity can be attributed to dATP first binding the specificity site, which stimulates CDP reduction, followed by dATP binding to the activity-regulating site causing inhibition. In contrast, titration of ATP leads to a steady increase in turnover up to 3 mM ATP (Figure 2F), and then maintenance of this high level of activity out to 10 mM ATP (Figure S7), the maximum concentration of ATP we tested. This trend in activity data is as expected from a positive effector and is consistent with recent work on murine RNR.[16]

Before comparing these activity data collected in the presence of both α and β (both subunits are required for activity) with oligomeric state data on α alone, the influence of β on the oligomeric state of α must be established. If, in the presence of dATP, β has no effect on the oligomeric state of α, then Figure 2 data can be interpreted as indicating that α_6 formation and inhibition are correlated (Figure 2B,C). As we describe below, we find this correlation to be valid in the case of dATP. In the presence of ATP, however, we show below that the presence of β does affect the oligomeric state of α, and thus we cannot definitively say based on Figure 2E,F data that ATP-induced α_6 are active.

β Has a Large Effect on the Structure of α Oligomers in the Presence of ATP, but Not in the Presence of dATP. To address the affect of β on the structures of α oligomers, we prepared multiple-turnover reaction mixtures of the two subunits under both activating (3 mM ATP, 1 mM CDP, 5 mM DTT) and inhibiting conditions (50 μM dATP, 1 mM CDP, 5 mM DTT). Scattering was then measured immediately after a short incubation of the reaction mixtures. Here, DTT was used to reduce the redox active cysteines in α that are oxidized during each turnover. Under the activating conditions (3 mM ATP, 1 mM CDP, 5 mM DTT), we expect ~25% of the CDP to be converted to dCDP during the course of the SAXS measurement. As no changes in scattering were observed during the course of data collection, this low level of turnover does not appear to affect the structure or background scattering to an appreciable extent.

We find that addition of β_2 to α under inhibiting conditions (50 μM dATP, 1 mM CDP, 5 mM DTT) leads to a scattering curve (Figure 4A, red) that is greater in overall intensity but

DOI: 10.1021/acs.biochem.5b01207
Biochemistry 2016, 55, 373−381

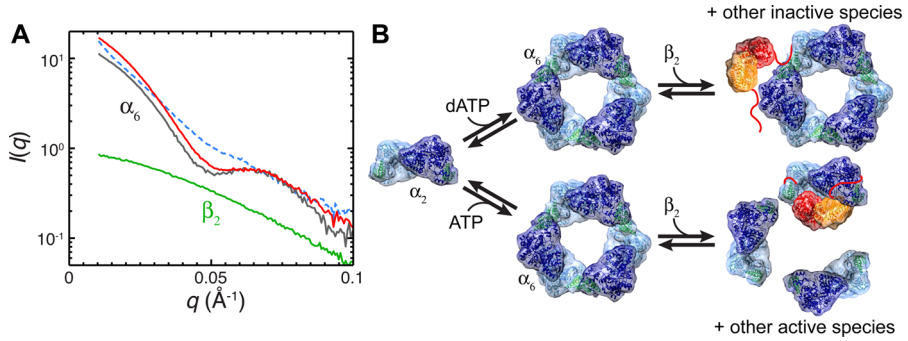

Figure 4. Human β can alter the structure of α oligomers substantially in the presence of activating effector, ATP, but not in the presence of dATP. (A) The dATP-induced α_6 (black) is represented by the SAXS profile of 4 μM α in 50 μM dATP, 1 mM CDP. Addition of equimolar β to 4 μM α under inhibitory conditions (50 μM dATP, 1 mM CDP, 5 mM DTT) results in scattering (red) that shares similar features as that of the dATP-induced α_6 (black). In contrast, addition of equimolar β to 4 μM α under activating conditions (3 mM ATP, 1 mM CDP, 5 mM DTT) leads to scattering (blue dotted) that deviates greatly from that of the dATP-induced α_6 (black). For reference, the scattering from 16 μM β in 1 mM CDP is shown in green, normalized by a factor of 4 to facilitate comparison with other curves. (B) Model for the differential ability of human β to affect the oligomeric state of human α. In human RNR, both ATP and dATP can promote the formation of ring-shaped α_6 in the absence of β_2. β_2 cannot disrupt the dATP-induced α_6 and hence has poor access to the active sites lining the interior of the ring-shaped α_6. By contrast, addition of β_2 can disrupt the ATP-induced α_6 ring. Although the active conformation is not yet known, it is plausible that the increased dynamics under active conditions allows for greater access of β_2 to the active sites.

otherwise highly similar to that of the dATP-induced α_6 ring alone (Figure 4A, black). Notably the peak at $q \approx 0.07$ Å^{-1}, which arises from the ring-shaped hexameric arrangement, remains unperturbed and thus suggests that the dATP-induced α_6 ring maintains its shape even with the addition of β_2. Interestingly, the scattering under these conditions (Figure 4A, red) cannot be explained as a simple sum of the scattering from the α_6 ring (Figure 4A, black) and free β_2 (Figure 4A, green), indicating that the two subunits associate. In particular, a 1.6-fold increase is observed in the forward scattering intensity or $I(0)$, which is larger than the expected value of 1.1 in the case where β_2 cannot associate with the dATP-induced α_6 ring but is smaller than the expected value of 2.3 in the case where three copies of β_2 fully associate with the α_6 ring to form a homogeneous solution of $\alpha_6\beta_6$. These results indicate that some fraction of β_2 is associated with the dATP-induced α_6 ring, which is consistent with previous GEMMA results that suggest a dATP-induced $\alpha_6\beta_2$ species in murine RNR[16] as well as an EM reconstruction of a dATP-induced species from *S. cerevisiae* RNR in which a single copy of β_2 appears bound to the α_6 ring.[12] Although in this *S. cerevisiae* RNR structure β_2 appeared to be inside the ring, our data on the human protein in solution is not consistent with an interior binding site for β_2. In particular, we observe an increase in radius of gyration (R_g) from 72.9 ± 1.7 to 79.3 ± 3.0 Å with the addition of β_2 (Figure S8), which cannot be explained by the formation of a $\alpha_6\beta_2$ complex, in which β_2 is bound within the ring as the predominant species. As R_g represents the root-mean-square distance of all electrons in a particle, binding of β_2 to the interior of the α_6 ring would lead to an overall decrease in apparent R_g, and this value would be further reduced by the presence of any unbound β_2. Thus, although we cannot definitively identify a single structure for the inhibited complex as the scattering from our dATP sample likely contains both free and associated β_2, we can say that an $\alpha_6\beta_2$ state with β_2 outside the ring is a likely component (Figure 4B).

In contrast to the small changes observed when β is added to dATP-inhibited hexamers (black to red curves in Figure 4A), the addition of 4 μM β to 4 μM α in the presence of ATP leads to a dramatically different scattering curve (Figure 4A, blue dotted). As in the case of the ATP-induced filaments, here, we see an upturn at low q and a loss of scattering features, indicating that there is aggregation-like behavior involving highly anisotropic species. Although β_2 may bind to α filaments, any scattering from smaller species (such as $\alpha_2\beta_2$) would be masked by the presence of aggregates, which scatter more strongly. Thus, we cannot unambiguously identify the active form. However, comparing the effects of the two activity-regulating effectors leads to the important observation that the dATP-induced α_6 maintains its shape in the presence of the β subunit, whereas the ATP-induced α_6 does not (Figure 4B). This difference may explain why both effectors can form similar hexameric rings and produce different outcomes in activity.

DISCUSSION

Since the first observations of nucleotide-dependent oligomerization in pioneering studies of class Ia RNRs,[20−23,41] studies by Cooperman and co-workers have spurred renewed interest in elucidating its role in allosteric activity regulation.[9−16,19,42] These studies have shown that eukaryotic RNRs form a different set of quaternary structures than the *E. coli* class Ia RNR and, in particular, demonstrate the need to better resolve the oligomerization states of the α subunit. In this present study, we used solution-based SAXS to monitor the conformational changes of human α as a function of ATP and dATP. Because scattering is additive at the dilute protein concentrations used in SAXS, the large data sets generated by the titration experiments allow for model-independent SVD analysis. From this analysis, we find that dATP induces a dimer−hexamer transition with no tetramer intermediate. In addition, a similar dimer−hexamer transition is seen at sub-millimolar ATP. Furthermore, both ATP and dATP induce a ring-shaped hexamer that is consistent with our low-resolution X-ray crystal structure (Figure 1B). Although structurally similar, however, the dATP-induced α_6 and the ATP-induced α_6 differ in their relative stabilities. Whereas the latter is easily disrupted by the presence of the β subunit or by high concentrations of ATP, the former maintains its ring structure even when β subunit is added.

DOI: 10.1021/acs.biochem.5b01207
Biochemistry 2016, 55, 373−381

The inability to detect tetramers between the dimeric and hexameric forms of α in our SAXS data would at first seem to contradict previous observations. Seminal studies performed on RNR subunits purified from Ehrlich tumor cells and calf thymus were the first to show that both dATP and ATP can produce higher order oligomers of α.[20,21,41] In these studies, less generalized forms of the Svedberg equation were used to estimate mass from the sedimentation coefficients ($s_{20,w}$), leading to its underestimation. Specifically, use of the Atassi-Gandhi approximation to the Svedberg equation[43] led to a tetrameric mass assignment to a 15.2 S species observed in calf thymus RNR treated with dATP.[21] In the case of murine RNR, use of the Svedberg equation for a smooth sphere[44] again led to the assignment of a tetrameric mass for the 16 S species observed in the presence of dATP and a hexameric mass for a broad 23 S peak observed in the presence of ATP.[11,13] However, both equations only apply to highly globular proteins. With the structural data now available from this work and others,[10,12] we know that α oligomers cannot be approximated as such. Using modern software for hydrodynamic calculations,[45] we find that the ring-shaped hexamer observed in our crystal structure has a theoretical $s_{20,w}$ value of ~16 S. This result strongly suggests that the previously observed 15−16 S species likely arose from ring-shaped α hexamers, whereas higher $s_{20,w}$ values would be consistent with our observations of α filament formation. Use of structural information in hydrodynamic calculations thus brings consensus to previously inconsistent observations.

With the absence of tetramers established in eukaryotic RNRs, we find that a major structural difference in human RNR observed with ATP or dATP is in the relative stabilities of α_6 rings. Despite differences in quaternary structure, our observations with human RNR are reminiscent of our previous observations with the *E. coli* class Ia RNR (Figure 5). In *E. coli* RNR, dATP is uniquely able to stabilize a single species: the ring-shaped $\alpha_4\beta_4$ complex (Figure 5).[9] Furthermore, due to its transient nature, the active $\alpha_2\beta_2$ complex in *E. coli* RNR readily interconverts with other species, including $\alpha_4\beta_4$, under activating conditions.[9,14] Similarly, our results suggest that the α_6 ring forms the basis of the allosterically inhibited form of human RNR and that this species is able to interconvert with other species in the presence of ATP (Figure 5). Indeed, contrary to previously reported electron micrographs of the *S. cerevisiae* RNR (EM DataBank entry 1807), in which β_2 appeared to bind the interior of the α_6 ring,[12] our SAXS results suggest that such a configuration is not likely to be predominant in dATP-inhibited human RNR. We instead propose that the interior α_6 ring is largely inaccessible to β_2, particularly if we account for the presence of functionally essential tails in both subunits that are disordered and thus not visible in existing crystal structures. Modeling the disordered C-terminal tails of α within the α_6 ring not only reduces the accessibility of the active sites, but also further improves the agreement between the theoretical and experimental scattering (Figure S9 and Supporting Information). Our results thus suggest that in both *E. coli* and human RNR, allosteric inhibition entails keeping β_2 away from catalytic positions on α, either by forming a ring structure with β to hold it "at arm's length" or by forming a ring without β, such that β is excluded (Figure 5). Although the oligomeric states involved are not conserved between these two RNR species, the net result is the same: β is prevented from providing a radical species necessary to initiate catalysis in the active site of α.

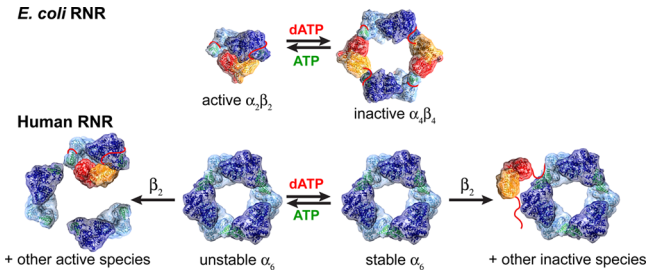

Figure 5. Model for the interconversion of oligomerization states in *E. coli* class Ia RNR compared with that of human RNR. In *E. coli* RNR, α_2 does not form higher order oligomers without β_2. Addition of dATP and β_2 leads to a ring-shaped $\alpha_4\beta_4$, which prevents β_2 from interacting with the active site of α_2 ("β_2 held at arm's length" model), whereas addition of ATP favors a compact $\alpha_2\beta_2$ complex that is active. In human RNR, α forms higher order oligomers without β_2. Both ATP and dATP cause α to hexamerize, but these hexamers have variable stability. The increased stability of dATP-induced α_6 prevents β_2 from gaining access to the active site of α_2 ("β_2 exclusion" model), whereas the decreased stability of ATP-induced α_6 allows β_2 access to the active site of α_2, creating active RNR species.

Our results serve to elucidate the structural basis of allosteric inhibition in human RNR, and at the same time, raise a number of fascinating questions. Specifically, we observe mixtures of species in the presence of both subunits and ATP, some or all of which could be physiologically relevant and/or catalytically active. Although the physiological relevance of α filaments remains to be seen, with the recent visualization of filamentous states of CTP synthetase and IMP dehydrogenase in cells,[46,47] a case can be made for exploring whether filaments observed in vitro can also exist in vivo. Understanding the relevance of RNR oligomeric states as well as the kinetics of structural interconversions will ultimately be essential for understanding RNR function. With the recent progress made for eukaryotic RNRs from this work and others,[10−12,15,16] we are entering a new phase of discovery into this complex class of enzymes.

■ ASSOCIATED CONTENT

Supporting Information

The Supporting Information is available free of charge on the ACS Publications website at DOI: 10.1021/acs.biochem.5b01207.

Detailed methods, crystallographic data collection and refinement statistics, SAXS shape reconstruction statistics, and additional figures depicting crystal packing of previous structure of yeast α_6, electron density map of human α_6 structure, analysis of SAXS data, and activity assay data (PDF)

■ AUTHOR INFORMATION

Corresponding Authors

*(N.A.) Phone: 609-258-6513. E-mail: nozomi.ando@princeton.edu.

*(C.L.D.) Phone: 617-253-5622. E-mail: cdrennan@mit.edu.

Present Address

⊥Department of Chemistry, Princeton University, Princeton, NJ 08544.

Author Contributions

#N.A. and H.L. contributed equally to this work.

DOI: 10.1021/acs.biochem.5b01207
Biochemistry 2016, 55, 373−381

Funding

This work was supported by the National Institutes of Health Grants GM100008 (N.A.) and GM29595 (J.S.) and MIT's Undergraduate Research Opportunities Program (M.I.M., J.E.P., and S.T.). C.L.D. is a Howard Hughes Medical Institute Investigator. SAXS and crystallography data collection were conducted at the Cornell High Energy Synchrotron Source (CHESS), which is supported by the National Science Foundation Award DMR-1332208, using the Macromolecular Diffraction at CHESS (MacCHESS) facility, which is supported by award GM-103485 from the National Institute of General Medical Sciences, National Institutes of Health.

Notes

The authors declare no competing financial interest.

■ ACKNOWLEDGMENTS

We thank Chae Un Kim (CHESS/UNIST) for assistance with the collection of diffraction data that yielded crystal structure, Yimon Aye (Cornell) for purifying the sample that was used in crystallization and EM, and Marco Jost (MIT) and Bob Grant (MIT) for assistance with data processing and refinement. We are grateful to Richard Gillilan (CHESS) for setting up the SAXS flow cell and robotics, Cynthia Kinsland (Cornell) for providing advice on purification, and Michael Funk for assistance with the preparation of electron microscopy specimens.

■ ABBREVIATIONS

RNR, ribonucleotide reductase; ATP, adenosine 5′-triphosphate; dATP, deoxyadenosine 5′-triphosphate; CDP, cytidine 5′-diphosphate; AUC, analytical ultracentrifugation; SAXS, small-angle X-ray scattering; EM, electron microscopy; SVD, singular value decomposition; R_g, radius of gyration; R_c, cross-sectional radius of gyration

■ REFERENCES

(1) Hofer, A., Crona, M., Logan, D. T., and Sjöberg, B.-M. (2012) DNA building blocks: keeping control of manufacture. *Crit. Rev. Biochem. Mol. Biol. 47*, 50−63.

(2) Jordan, A., and Reichard, P. (1998) Ribonucleotide reductases. *Annu. Rev. Biochem. 67*, 71−98.

(3) Nordlund, P., and Reichard, P. (2006) Ribonucleotide reductases. *Annu. Rev. Biochem. 75*, 681−706.

(4) Aye, Y., Li, M., Long, M. J. C., and Weiss, R. S. (2015) Ribonucleotide reductase and cancer: biological mechanisms and targeted therapies. *Oncogene 34*, 2011−2021.

(5) Shao, J., Zhou, B., Chu, B., and Yen, Y. (2006) Ribonucleotide reductase inhibitors and future drug design. *Curr. Cancer Drug Targets 6*, 409−431.

(6) Stubbe, J. (1998) Ribonucleotide reductases in the twenty-first century. *Proc. Natl. Acad. Sci. U. S. A. 95*, 2723−2724.

(7) Minnihan, E. C., Nocera, D. G., and Stubbe, J. (2013) Reversible, long-range radical transfer in *E. coli* class Ia ribonucleotide reductase. *Acc. Chem. Res. 46*, 2524−2535.

(8) Licht, S., Gerfen, G. J., and Stubbe, J. (1996) Thiyl radicals in ribonucleotide reductases. *Science 271*, 477−481.

(9) Ando, N., Brignole, E. J., Zimanyi, C. M., Funk, M. A., Yokoyama, K., Asturias, F. J., Stubbe, J., and Drennan, C. L. (2011) Structural interconversions modulate activity of *Escherichia coli* ribonucleotide reductase. *Proc. Natl. Acad. Sci. U. S. A. 108*, 21046−21051.

(10) Aye, Y., and Stubbe, J. (2011) Clofarabine 5′-di and -triphosphates inhibit human ribonucleotide reductase by altering the quaternary structure of its large subunit. *Proc. Natl. Acad. Sci. U. S. A. 108*, 9815−9820.

(11) Cooperman, B. S., and Kashlan, O. B. (2003) A comprehensive model for the allosteric regulation of Class Ia ribonucleotide reductases. *Adv. Enzyme Regul. 43*, 167−182.

(12) Fairman, J. W., Wijerathna, S. R., Ahmad, M. F., Xu, H., Nakano, R., Jha, S., Prendergast, J., Welin, R. M., Flodin, S., Roos, A., Nordlund, P., Li, Z., Walz, T., and Dealwis, C. G. (2011) Structural basis for allosteric regulation of human ribonucleotide reductase by nucleotide-induced oligomerization. *Nat. Struct. Mol. Biol. 18*, 316−322.

(13) Kashlan, O. B., Scott, C. P., Lear, J. D., and Cooperman, B. S. (2002) A comprehensive model for the allosteric regulation of mammalian ribonucleotide reductase. Functional consequences of ATP- and dATP-induced oligomerization of the large subunit. *Biochemistry 41*, 462−474.

(14) Minnihan, E. C., Ando, N., Brignole, E. J., Olshansky, L., Chittuluru, J., Asturias, F. J., Drennan, C. L., Nocera, D. G., and Stubbe, J. (2013) Generation of a stable, aminotyrosyl radical-induced $\alpha 2\beta 2$ complex of *Escherichia coli* class Ia ribonucleotide reductase. *Proc. Natl. Acad. Sci. U. S. A. 110*, 3835−3840.

(15) Wang, J., Lohman, G. J. S., and Stubbe, J. (2007) Enhanced subunit interactions with gemcitabine-5′-diphosphate inhibit ribonucleotide reductases. *Proc. Natl. Acad. Sci. U. S. A. 104*, 14324−14329.

(16) Rofougaran, R., Vodnala, M., and Hofer, A. (2006) Enzymatically active mammalian ribonucleotide reductase exists primarily as an alpha6beta2 octamer. *J. Biol. Chem. 281*, 27705−27711.

(17) Jonna, V. R., Crona, M., Rofougaran, R., Lundin, D., Johansson, S., Brännström, K., Sjöberg, B.-M., and Hofer, A. (2015) Diversity in Overall Activity Regulation of Ribonucleotide Reductase. *J. Biol. Chem. 290*, 17339−17348.

(18) Uhlin, U., and Eklund, H. (1994) Structure of ribonucleotide reductase protein R1. *Nature 370*, 533−539.

(19) Zimanyi, C. M., Ando, N., Brignole, E. J., Asturias, F. J., Stubbe, J., and Drennan, C. L. (2012) Tangled Up in Knots: Structures of Inactivated Forms of *E. coli* Class Ia Ribonucleotide Reductase. *Structure 20*, 1374−1383.

(20) Klippenstein, G. L., and Cory, J. G. (1978) Ribonucleotide reductase: association of the regulatory subunit in the presence of allosteric effectors. *Biochem. Biophys. Res. Commun. 83*, 252−258.

(21) Thelander, L., Eriksson, S., and Akerman, M. (1980) Ribonucleotide reductase from calf thymus. Separation of the enzyme into two nonidentical subunits, proteins M1 and M2. *J. Biol. Chem. 255*, 7426−7432.

(22) Brown, N. C., and Reichard, P. (1969) Ribonucleoside diphosphate reductase* 1:: Formation of active and inactive complexes of proteins B1 and B2. *J. Mol. Biol. 46*, 25−38.

(23) Thelander, L. (1973) Physicochemical characterization of ribonucleoside diphosphate reductase from *Escherichia coli*. *J. Biol. Chem. 248*, 4591−4601.

(24) Wang, J., Lohman, G. J. S., and Stubbe, J. (2009) Mechanism of inactivation of human ribonucleotide reductase with p53R2 by gemcitabine 5′-diphosphate. *Biochemistry 48*, 11612−11621.

(25) Ando, N., Chenevier, P., Novak, M., Tate, M. W., and Gruner, S. M. (2008) High hydrostatic pressure small-angle X-ray scattering cell for protein solution studies featuring diamond windows and disposable sample cells. *J. Appl. Crystallogr. 41*, 167−175.

(26) Nielsen, S. S., Møller, M., and Gillilan, R. E. (2012) High-throughput biological small-angle X-ray scattering with a robotically loaded capillary cell. *J. Appl. Crystallogr. 45*, 213−223.

(27) Skou, S., Gillilan, R. E., and Ando, N. (2014) Synchrotron-based small-angle X-ray scattering of proteins in solution. *Nat. Protoc. 9*, 1727−1739.

(28) Firer-Sherwood, M. A. M. A., Ando, N. N., Drennan, C. L. C. L., and Elliott, S. J. S. J. (2011) Solution-based structural analysis of the decaheme cytochrome, MtrA, by small-angle X-ray scattering and analytical ultracentrifugation. *J. Phys. Chem. B 115*, 11208−11214.

(29) Glatter, O., and Kratky, O., Eds. (1982) *Small-Angle X-ray Scattering*; Academic Press, New York.

(30) Svergun, D. I. (1992) Determination of the regularization parameter in indirect-transform methods using perceptual criteria. *J. Appl. Crystallogr. 25*, 495−503.

DOI: 10.1021/acs.biochem.5b01207
Biochemistry 2016, 55, 373−381

(31) Franke, D., and Svergun, D. I. (2009) DAMMIF, a program for rapid *ab-initio* shape determination in small-angle scattering. *J. Appl. Crystallogr. 42*, 342−346.
(32) Svergun, D. I. (1999) Restoring low resolution structure of biological macromolecules from solution scattering using simulated annealing. *Biophys. J. 76*, 2879−2886.
(33) Volkov, V. V., and Svergun, D. I. (2003) Uniqueness of *ab initio* shape determination in small-angle scattering. *J. Appl. Crystallogr. 36*, 860−864.
(34) Schneidman-Duhovny, D., Hammel, M., and Sali, A. (2010) FoXS: a web server for rapid computation and fitting of SAXS profiles. *Nucleic Acids Res. 38*, W540−544.
(35) Fiser, A., Do, R. K., and Sali, A. (2000) Modeling of loops in protein structures. *Protein Sci. 9*, 1753−1773.
(36) Weinkam, P. P., Pons, J. J., and Sali, A. A. (2012) Structure-based model of allostery predicts coupling between distant sites. *Proc. Natl. Acad. Sci. U. S. A. 109*, 4875−4880.
(37) Dubochet, J., Ducommun, M., Zollinger, M., and Kellenberger, E. (1971) A new preparation method for dark-field electron microscopy of biomacromolecules. *J. Ultrastruct. Res. 35*, 147−167.
(38) Tischendorf, G. W., Zeichhardt, H., and Stoffler, G. (1974) Determination of the location of proteins L14, L17, L18, L19, L22 and L23 on the surface of the 50S ribosomal subunit of *Escherichia coli* by immune electron microscopy. *Mol. Gen. Genet. 134*, 187−208.
(39) Hakansson, P., Hofer, A., and Thelander, L. (2006) Regulation of Mammalian Ribonucleotide Reduction and dNTP Pools after DNA Damage and in Resting Cells. *J. Biol. Chem. 281*, 7834−7841.
(40) Reichard, P., Eliasson, R., Ingemarson, R., and Thelander, L. (2000) Cross-talk between the allosteric effector-binding sites in mouse ribonucleotide reductase. *J. Biol. Chem. 275*, 33021−33026.
(41) Engström, Y., Eriksson, S., Thelander, L., and Akerman, M. (1979) Ribonucleotide reductase from calf thymus. Purification and properties. *Biochemistry 18*, 2941−2948.
(42) Rofougaran, R., Crona, M., Vodnala, M., Sjöberg, B.-M., and Hofer, A. (2008) Oligomerization status directs overall activity regulation of the *Escherichia coli* class Ia ribonucleotide reductase. *J. Biol. Chem. 283*, 35310−35318.
(43) Halsall, H. B. (1967) Atassi−Gandhi Sedimentation Coefficient and Molecular Weight Relationships. *Nature 215*, 880−881.
(44) Cantor, C. R., and Schimmel, P. R. (1980) *Biophysical Chemistry: Techniques for the Study of Biological Structure and Function*, W. H. Freeman, San Francisco.
(45) Brookes, E., Demeler, B., Rosano, C., and Rocco, M. (2010) The implementation of SOMO (SOlution MOdeller) in the UltraScan analytical ultracentrifugation data analysis suite: enhanced capabilities allow the reliable hydrodynamic modeling of virtually any kind of biomacromolecule. *Eur. Biophys. J. 39*, 423−435.
(46) Barry, R. M., Bitbol, A.-F., Lorestani, A., Charles, E. J., Habrian, C. H., Hansen, J. M., Li, H.-J., Baldwin, E. P., Wingreen, N. S., Kollman, J. M., and Gitai, Z. (2014) Large-scale filament formation inhibits the activity of CTP synthetase. *eLife 3*, e03638.
(47) Zhao, H., Chiaro, C. R., Zhang, L., Smith, P. B., Chan, C. Y., Pedley, A. M., Pugh, R. J., French, J. B., Patterson, A. D., and Benkovic, S. J. (2015) Quantitative analysis of purine nucleotides indicates that purinosomes increase de novo purine biosynthesis. *J. Biol. Chem. 290*, 6705−6713.

DOI: 10.1021/acs.biochem.5b01207
Biochemistry 2016, 55, 373−381